International Journal of Coal Science & Technology (2024) 11:2
https://doi.org/10.1007/s40789-023-00626-0

RESEARCH

Numerical analysis on the factors affecting post-peak characteristics of coal under uniaxial compression

Zhiguo Lu[1,2] · Wenjun Ju[1,2] · Fuqiang Gao[1,2] · Taotao Du[1,2]

Received: 8 April 2023 / Revised: 8 July 2023 / Accepted: 10 August 2023

Abstract

The post-peak characteristics of coal serve as a direct reflection of its failure process and are essential parameters for evaluating brittleness and bursting liability. Understanding the significant factors that influence post-peak characteristics can offer valuable insights for the prevention of coal bursts. In this study, the Synthetic Rock Mass method is employed to establish a numerical model, and the factors affecting coal post-peak characteristics are analyzed from four perspectives: coal matrix mechanical parameters, structural weak surface properties, height-to-width ratio, and loading rate. The research identifies four significant influencing factors: deformation modulus, density of discrete fracture networks, height-to-width ratio, and loading rate. The response and sensitivity of post-peak characteristics to single-factor and multi-factor interactions are assessed. The result suggested that feasible prevention and control measures for coal bursts can be formulated through four approaches: weakening the mechanical properties of coal pillars, increasing the number of structural weak surfaces in coal pillars, reducing the width of coal pillars, and optimizing mining and excavation speed. The efficacy of measures aimed at weakening the mechanical properties of coal is successfully demonstrated through a case study on coal burst prevention using large-diameter borehole drilling.

Keywords Post-peak behavior · Synthetic rock mass · Coal bursts · Coal burst prevention

1 Introduction

Post-peak characteristics serve as a direct representation of coal's damage process and play a critical role in evaluating the brittleness and bursting liability of coal materials (Kuang et al. 2021). In laboratory assessments of coal sample bursting liability, the complete stress–strain curve obtained from uniaxial compression is a vital parameter for determining bursting liability evaluation indices, such as the impact energy index and the residual elastic energy index. In coal mining engineering practices, the failure pattern (stable or unstable) of coal is dictated by both local mine stiffness and post-peak characteristics of coal. According to the local mine stiffness theory, unstable damage (e.g., dynamic hazards like impact ground pressure) occurs when the local mine stiffness (LMS) is smaller than the slope of the coal's post-peak curve, the loading system stiffness is less than the coal stiffness, and the applied energy of the loading system surpasses the damage absorption energy of coal (Gao et al. 2019; Salamon 1970). Comprehending the post-peak characteristics of coal is of paramount importance for preventing coal bursts.

Post-peak characteristics of coal can be quantitatively characterized based on variations in load, deformation, energy, or their interrelationships. The post-peak modulus (M) represents the rate of stress reduction with increasing strain during the post-peak phase and serves as a prevalent quantitative evaluation index for post-peak characteristics (Tarasov and Potvin 2013a, b; Tarasov and Randolph 2011; Ai et al. 2016; Li et al. 2018). However, the rate of post-peak stress reduction with strain is not constant and varies significantly. In applications, M is typically characterized by the slope of the line connecting the peak strength and residual strength in the stress–strain curve (Zhou et al. 2018; Kivi et al. 2018; Xia et al. 2017; Meng et al. 2014). Post-peak mechanical properties are crucial in geoengineering stability (Cai et al. 2007; Alonso et al. 2003), with residual

✉ Fuqiang Gao
fuqgao@gmail.com

1 CCTEG Coal Mining Research Institute, Beijing, China

2 State Key Laboratory of Coal Intelligent Mining and Strata Control (China Coal Research Institute), Beijing, China

Published online: 04 January 2024

strength being another common post-peak characterization parameter. The greater the residual strength, the lower the post-peak stress reduction rate, and the smaller the post-peak modulus reduction (Han et al. 2012). Numerous studies have investigated the effect of confining pressure on residual strength. Peng et al. (2017) introduced the strength degradation index to describe the post-peak curve and proposed a negative exponential relationship between confining pressure and strength degradation index. Yang et al. (2012) conducted a "reducing confining pressure" experiment, demonstrating that the post-peak axial strain varies considerably with confining pressure, and the post-peak residual strength exhibits a strong linear relationship with confining pressure. The post-peak energy evolution law is an essential aspect of post-peak characteristics research and a crucial parameter in the quantitative evaluation of post-peak characteristics (Zhang and Li 2019). Analyzing post-peak characteristics from an energy perspective is vital for understanding coal burst mechanisms and prevention (Akdag et al. 2019).

The post-peak characteristics of coal under compression are influenced not only by the content of internal mineral components and their mechanical properties (Wang and Gale 2009; Jarvie et al. 2007; Hajiabdolmajid et al. 2002), but also by environmental factors such as water, temperature, specimen size, surrounding pressure, loading rate, cyclic loading, and unloading paths and several cycles. The softening and dissolution effects of water diminish the mechanical properties of the coal rock mass and alter the damage mode of coal rock, with increased water content resulting in greater energy dissipation through permanent plastic deformation during the post-peak stage, reducing brittleness and bursting liability (Liu et al. 2021; Meng et al. 2009). Peng et al. (2016) investigated the impact of temperature on the physical and mechanical properties of coarse marble, finding that the failure pattern transitions from brittle to ductile as processing temperature increases. Yao et al. (2016) conducted triaxial compression experiments on coarse marble after high-temperature treatment to analyze the effects of thermal damage and the coupling effect of surrounding pressure on post-peak characteristics. They found that with increasing surrounding pressure, coarse marble transitions from brittle to ductile, with the thermal effect enhancing ductility. Test conditions directly affect coal sample post-peak characteristics, with surrounding pressure's influence on post-peak characteristics being most extensively studied (Zhang and Li 2019; Akdag et al. 2019; Peng et al. 2017; Yao et al. 2016; Meng et al. 2014; Yang et al. 2012; Han et al. 2012). As surrounding pressure increases, post-peak residual strength rises and the stress reduction rate slows down. Consequently, the energy dissipation during the post-peak damage process increases, transitioning from brittle to ductile damage. Yang et al. (2017) conducted post-peak uniaxial and triaxial cyclic loading and unloading experiments on sandstones, discovering that rock deterioration intensifies as the number of cycles increases. Additionally, input energy, dissipated energy, and stored elastic energy in the post-peak stage decrease, while the area of the plastic hysteresis loop diminishes. Zhang et al. (2022) conducted triaxial cyclic loading and unloading experiments to analyze the influence of confining pressure and temperature simultaneously. They concluded that limestone's failure mode changes from brittleness to ductility with the increase of confining pressure and temperature.

Coal is abundant in primary defects, such as bedding planes, butt cleats, and face cleats, which significantly impact the mechanical properties of coal. Wang et al. (2014) used segmented linear functions to describe the evolution of post-peak mechanical parameters with maximum principal strain, analyzing the post-peak characteristics of jointed rock masses. Cheng (2011) numerically simulated intermittent jointed rock samples with varying numbers and extension directions, finding that the post-peak modulus decreases as the number of joints increases. When the joint dip angle is 60°, the numerical model exhibits shear slip along the joint, resulting in the smallest post-peak modulus and weakest brittleness. Ai et al. (2016) assessed the post-peak brittleness characteristics of red sandstone, granite, and black shale from an energy evolution perspective and studied the anisotropy of post-peak characteristics of black shale. The anisotropy of the post-peak characteristics of shale indicates that brittleness increases as the angle between the bedding planes and the loading direction decreases. Xu and Cai (2017) employed finite element numerical analysis to study the effect of loading system stiffness on the characteristics of the post-peak curve under uniaxial compression. They discovered that the slope of the post-peak curve decreases with increasing stiffness of the loading system, and rock instability damage can be suppressed when the stiffness of the loading system is sufficiently large.

The post-peak behavior of rocks is affected by various factors, which can be categorized into controllable and uncontrollable factors based on their potential for artificial alteration. When mining longwall panels, it is challenging to control environmental factors like moisture and temperature, pre-mining stress, and the repeated loading and unloading cycles experienced by coal pillars. However, the physical and mechanical properties of coal pillars can be modified artificially through techniques like hydraulic fracturing and grouting. The height and width-to-height ratio of coal pillars can also be adjusted. The rate at which the longwall face advances has a direct impact on the loading and unloading rate of coal pillars. Although previous studies on post-peak characteristics have primarily focused on dense rocks such as sandstone, marble, and granite, pillar bursts are the most common form of coal bursts in coal mines. Effective control of post-peak characteristics can reduce the risk of such occurrences. Therefore, understanding the factors that influence the post-peak characteristics of coal and identifying controllable factors is crucial for targeted control measures.

Conducting compression tests on large-scale coal samples in situ is impractical due to the difficulty of sampling, lack of loading equipment, and high costs. Therefore, in this study, the Synthetic Rock Mass (SRM) method was utilized to create a jointed coal model. This approach aimed to evaluate the factors that influence post-peak characteristics from four perspectives, namely matrix mechanical parameters, structural surface characteristics, height-to-width ratio, and loading rate. The study also aimed to investigate the response patterns of post-peak characteristics to single and multi-factor interactions.

2 Numerical simulation scheme based on response surface method

2.1 Model configuration

The Bonded Particle Model (BPM) was utilized to simulate the behavior of coal matrix using the Itasca's PFC2D numerical simulation software (Itasca Consulting Group Inc 2016). The distribution of internal structural defects within coal samples was obtained by binarization of CT scanning results. Based on this information, a non-uniform Discrete Fracture Network (DFN) grid model was developed to characterize the original defects of coal samples. The behavior of the DFN was simulated using the Smooth Joint Model (SJM). By combining the coal matrix and defects, the SRM numerical core of the rock mass was generated, enabling the more accurate characterization of the heterogeneous characteristics of coal, as depicted in Fig. 1. The effectiveness of the SRM method in characterizing the non-homogeneous features of jointed rock masses has been widely demonstrated.

The SRM model was calibrated to the laboratory-tested results of coal samples by conducting uniaxial compression tests using a trial-and-error approach, as reported in a study by Lu et al. (2019). The calibrated parameters of the SRM model are provided in Table 1. A direct comparison of the axial stress-axial strain curves between the laboratory results and the SRM model is illustrated in Fig. 2. The comparison reveals that the SRM model realistically represents the behavior of coal (see Table 2).

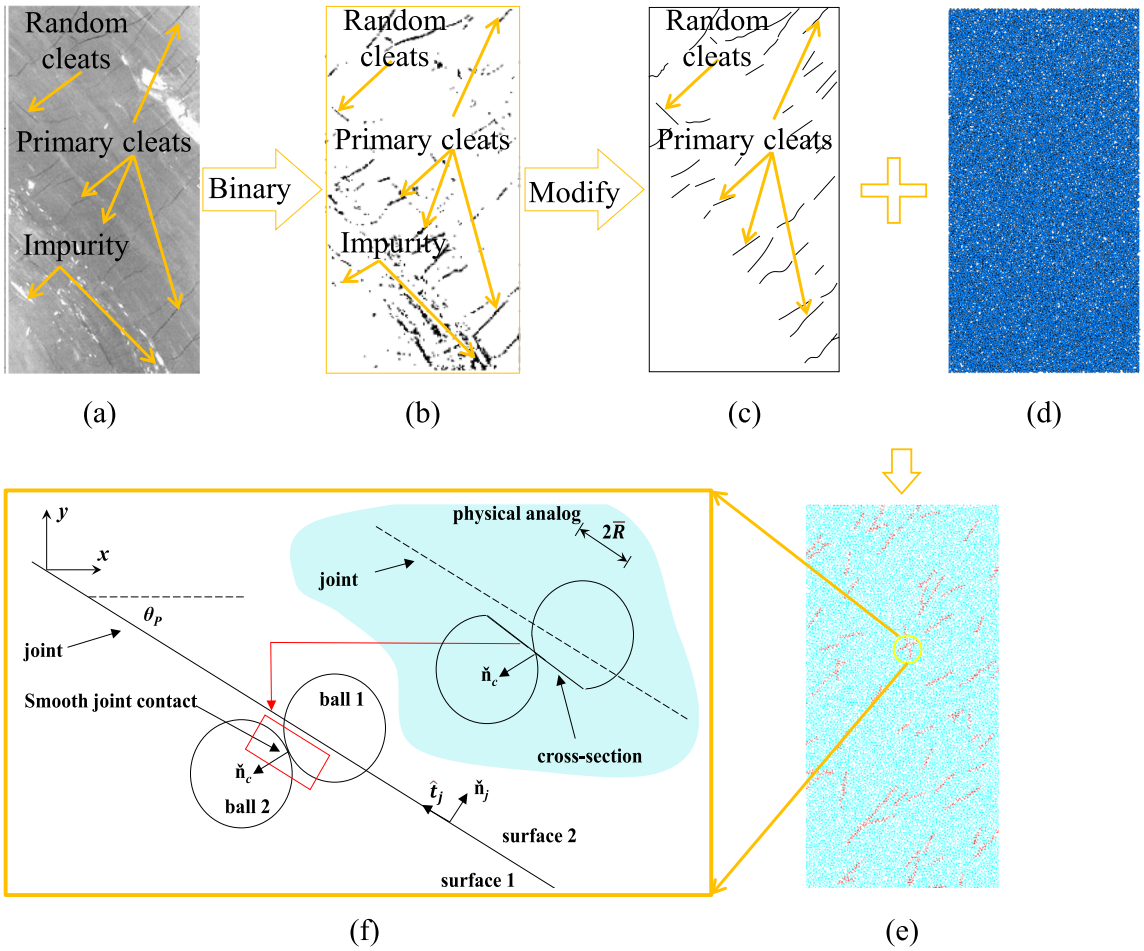

Fig. 1 The process of SRM model generation. **a** CT scan **b** Binaryzation **c** Modified DFN **d** Bonded particle model **e** SRM model **f** Notations used to defined joint and smooth joint contact

Table 1 Calibrated mesoscopic parameter of coal SRM model used in this study

Object	Parameter	Dimension	Magnitude
Ball	Density	kg/m^3	2500
	Radius	mm	0.25–0.5
	Porosity	–	0.1
	Damping Coefficient	–	0.7
Parallel bond model (PBM)	Cohesion	MPa	22.8
	Tensile strength	MPa	25.3
	Angle of internal friction	°	30.0
	Normal stiffness/Shear stiffness	–	5.0
	Deformation modulus	GPa	1.31
Smooth joint model (SJM)	Normal stiffness	GPa/m	1.5
	Shear stiffness	GPa/m	0.8
	Friction coefficient	–	0.577
	Tensile strength	MPa	0
	Cohesion	MPa	0
	DFN density	–	50

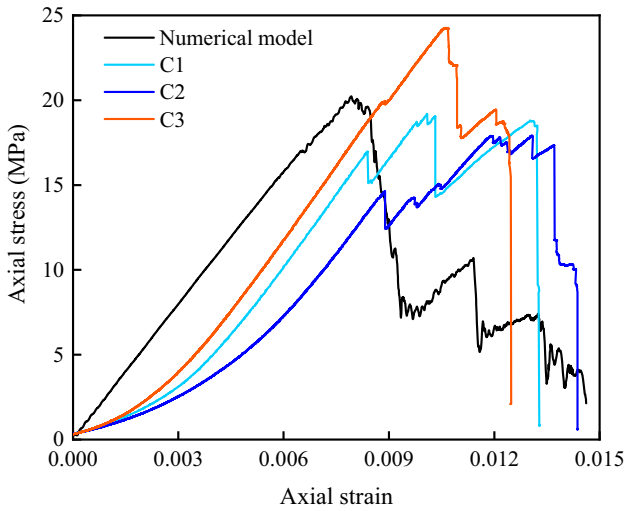

Fig. 2 Comparison of stress–strain curves between laboratory results and numerical results

The numerical core was found to exhibit uniaxial compressive strength (UCS) and elastic modulus values that were consistent with the results obtained from laboratory testing of coal samples. Furthermore, the stress–strain curve shape of the numerical core closely resembled that of the coal samples, especially in the post-peak regime. During loading, the post-peak stress exhibited a stepwise decrease (after reaching a peak strength, it abruptly dropped to a certain value, maintained, slowly rose or fell for a while, and then dropped to a lower value again). The comparison between numerical simulation and laboratory test results effectively validated the reliability of the calibration parameters used in the numerical model. Hence, the calibration parameters can be utilized to analyze the factors influencing the post-peak characteristics of the stress–strain curve of coal samples. It is important to note that the numerically-simulated stress–strain curve did not exhibit the initial bedding and crack closure stages observed in the laboratory-tested curves at the initial stage of loading. Because this phenomenon has almost no effect on the post-peak characteristics, it was not accounted for in the numerical model.

2.2 Modeling strategy and result

The mechanical response of coal under compression is influenced not only by the mechanical properties of the coal matrix and the spatial distribution and mechanical

Table 2 Comparison of experimental and numerical results

Item	Experiment result				Simulation result	Absolute error	Relative error
	C1	C2	C3	Mean			
Uniaxial compressive strength (UCS) (MPa)	18.81	17.91	24.27	20.33	20.24	0.09	0.44
Elastic modulus	2.757	2.430	2.881	2.69	2.63	0.06	2.23

characteristics of structural weak surfaces, but also by the size of the tested sample and the loading conditions. To investigate the influence of these factors on post-peak characteristics, different height-to-width models were constructed by altering the height of the numerical model, and different loading rates were achieved by adjusting calculation time steps. The SRM model characterized the coal matrix and pre-existing discontinuities using bonded particles and DFN, respectively. Six typical influencing factors were selected to analyze the post-peak characteristics curve of coal samples under uniaxial compression, including deformation modulus, tensile strength, and cohesion of PBM, as well as fracture density, shear modulus, and friction coefficient of DFN. Additionally, the influence of height-to-width ratio and loading rate was evaluated. The range of each factor considered in the sensitivity study is presented in Table 3.

The orthogonal design method was used to evaluate the comparative effectiveness of multiple intervention components on the post-peak behavior of coal (Feng et al. 2016; Li et al. 2016). A total of 120 numerical models were conducted to perform 8-factor, 3-level tests. The coding and level settings of each factor are shown in Table 3. Figure 3 illustrates a typical stress–strain curve of the SRM under uniaxial compression, wherein the post-peak curve exhibits a step-like decrease (after the peak intensity drops suddenly to a certain value, it either remains, or slowly rises, or slowly decreases for a period of time before dropping suddenly to a lower value again), similar to that obtained from laboratory tests. The post-peak drop modulus M for this model was defined as the absolute value of the slope obtained by connecting the peak stress to the final stress. The post-peak energy density U, which characterizes the energy dissipated during the damage of coal samples, was obtained by calculating the area enclosed by the full stress–strain post-peak curve and the horizontal axis (strain axis). M and U were used to quantitatively evaluate the post-peak characteristics of the SRM under uniaxial compression (Zhou et al. 2018; Kivi et al. 2018; Xia et al. 2017; Meng et al. 2014).

Table 4 provides input data and results obtained from all 120 tests.

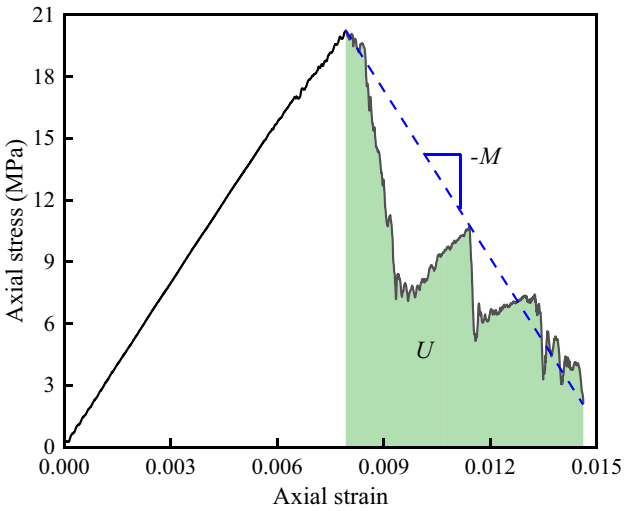

Fig. 3 Calculation of the post-peak modulus and energy density from the complete stress–strain curve obtained from uniaxial compressive tests

3 Analysis of factors influencing the post-peak modulus *M*

The P-value represents the level of significance of each factor on the experimental results. If $P < 0.05$, then the factor has a significant influence on the experimental results. If $P < 0.0001$, it indicates that the factor has a very significant influence on the experimental results. Table 5 presents the variance analysis of the regression model of the factors influencing M. The P-value of less than 0.0001 indicates that the regression effect is highly significant. The F-value in the regression model is inversely related to the P-value, with the height-to-width ratio having the highest F-value, indicating that this factor has the most significant effect on the M of coal samples among the eight factors selected. Based on decreasing F-values, the sensitivity of the response of M to three very significant and one significant influencing factors is in the order of height-to-width ratio > SJM DFN density > loading rate > PBM deformation modulus.

Table 3 Value ranges of factors influencing the post-peak characteristics of coal

Coded value	PBM			DFN model			Model size	Loading condition
	A (GPa)	*B* (MPa)	*C* (MPa)	*D*	*E* (GPa)	*F*	*G*	*H* (10^{-8} m/step)
−1	1.12	23.6	21.6	40	0.6	0.364	1	3.0
0	1.31	25.3	22.8	50	0.8	0.577	2	4.0
1	1.50	27.0	24.0	60	1.0	0.839	3	5.0

A-PBM deformation modulus, *B*-PBM tensile strength, *C*-PBM cohesion, *D*-SJM DFN density, *E*-SJM shear stiffness, *F*-SJM friction coefficient, *G*-Height-to-width ratio, *H*-Loading rate

Table 4 Numerical results of 120 tests of evaluating factors affecting the post-peak behavior of coal under unconfined compression

No.	*A* (GPa)	*B* (MPa)	*C* (MPa)	*D*	*E* (GPa)	*F*	*G*	*H* (10^{-8} m/step)	*M* (GPa)	*U* (μJ/mm^3)
1	3.00	25.3	21.6	50	0.8	0.839	2	3.0	6.8318	13.4189
2	1.31	25.3	22.8	50	0.8	0.577	2	4.0	9.2144	22.4371
3	1.31	27.0	21.6	50	0.8	0.839	1	4.0	22.575	17.2852
4	1.12	25.3	21.6	50	0.8	0.364	2	3.0	10.277	23.6532
5	1.12	27.0	22.8	50	0.6	0.839	2	4.0	8.1324	33.5200
6	1.12	23.6	22.8	50	0.6	0.364	2	4.0	13.111	33.2038
7	1.31	23.6	21.6	50	0.8	0.364	1	4.0	20.607	14.5847
8	3.00	25.3	24.0	50	1.0	0.577	3	4.0	28.453	18.1134
9	3.00	25.3	22.8	40	1.0	0.577	2	3.0	24.096	17.0157
10	3.00	25.3	22.8	60	0.6	0.577	2	3.0	11.577	26.0702
11	1.31	25.3	24.0	40	0.8	0.577	1	5.0	29.996	12.8794
12	1.31	27.0	22.8	60	0.8	0.839	2	5.0	12.376	37.5785
13	1.31	27.0	21.6	50	1.0	0.577	2	3.0	15.976	33.7459
14	1.31	25.3	22.8	50	0.8	0.577	2	4.0	10.029	20.6309
15	1.31	23.6	24.0	50	0.8	0.839	1	4.0	12.409	17.6383
16	1.31	27.0	22.8	60	1.0	0.577	3	4.0	6.488	33.9463
17	1.12	25.3	24.0	50	0.8	0.364	2	5.0	10.093	23.4708
18	1.31	27.0	22.8	40	1.0	0.577	1	4.0	19.716	16.1012
19	1.31	25.3	22.8	50	0.8	0.577	2	4.0	15.956	26.4378
20	1.31	27.0	22.8	40	0.8	0.839	2	3.0	12.286	21.9373
21	1.31	25.3	21.6	40	0.6	0.364	2	4.0	9.4729	17.9531
22	1.31	27.0	22.8	40	0.8	0.364	2	5.0	29.724	17.1270
23	1.31	23.6	22.8	40	0.6	0.577	1	4.0	23.469	15.2511
24	1.31	27.0	24.0	50	0.8	0.839	3	4.0	15.268	37.2991
25	1.31	25.3	21.6	40	1.0	0.839	2	4.0	15.869	16.3759
26	3.00	25.3	22.8	60	0.8	0.839	3	4.0	6.3553	18.3346
27	3.00	27.0	22.8	50	0.8	0.577	3	5.0	15.379	20.1607
28	1.31	23.6	24.0	50	0.8	0.364	3	4.0	7.594	33.0649
29	1.31	23.6	22.8	40	1.0	0.577	3	4.0	14.616	23.4451
30	1.31	25.3	21.6	60	0.8	0.577	1	5.0	12.714	17.2267
31	1.31	25.3	24.0	40	1.0	0.364	2	4.0	11.461	18.8303
32	3.00	25.3	22.8	40	0.8	0.839	1	4.0	24.752	11.2630
33	1.31	25.3	24.0	40	0.8	0.577	3	3.0	19.770	15.9414
34	1.31	25.3	22.8	50	0.8	0.577	2	4.0	8.002	40.0648
35	3.00	27.0	24.0	60	0.8	0.577	2	4.0	14.522	21.0612
36	3.00	27.0	22.8	50	0.6	0.364	2	4.0	13.944	13.6824
37	1.31	25.3	22.8	50	0.6	0.364	3	5.0	11.842	15.9547
38	1.12	25.3	22.8	60	1.0	0.577	2	3.0	2.023	32.1113
39	1.31	25.3	22.8	50	1.0	0.364	1	5.0	26.006	7.3714
40	1.12	27.0	22.8	50	0.8	0.577	3	3.0	3.900	64.0685
41	1.12	23.6	24.0	60	0.8	0.577	2	4.0	8.249	25.0894
42	1.31	27.0	21.6	50	0.6	0.577	2	5.0	11.277	18.2049
43	1.12	27.0	22.8	50	0.8	0.577	1	5.0	34.587	13.6277
44	3.00	25.3	22.8	40	0.8	0.364	3	4.0	10.932	19.4080
45	1.12	25.3	22.8	60	0.8	0.839	1	4.0	10.812	29.0640
46	1.31	27.0	24.0	50	0.8	0.364	1	4.0	24.189	5.9156
47	1.31	23.6	24.0	50	1.0	0.577	2	3.0	12.731	14.3214
48	1.12	23.6	22.8	50	0.8	0.577	1	3.0	7.619	27.0907
49	1.31	25.3	21.6	60	1.0	0.364	2	4.0	10.641	23.0658

Table 4 (continued)

No.	*A* (GPa)	*B* (MPa)	*C* (MPa)	*D*	*E* (GPa)	*F*	*G*	*H* (10^{-8} m/step)	*M* (GPa)	*U* (μJ/mm^3)
50	1.31	23.6	22.8	60	0.8	0.839	2	3.0	11.728	40.9257
51	3.00	25.3	24.0	50	0.8	0.839	2	5.0	17.200	12.9017
52	3.00	23.6	24.0	40	0.8	0.577	2	4.0	17.534	16.8020
53	1.31	25.3	24.0	60	0.8	0.577	3	5.0	10.9446	29.5918
54	1.12	25.3	24.0	50	0.8	0.839	2	3.0	7.655	29.2447
55	3.00	27.0	22.8	50	1.0	0.839	2	4.0	13.118	15.5332
56	1.31	27.0	24.0	50	1.0	0.577	2	5.0	14.938	14.8514
57	1.31	25.3	22.8	50	0.8	0.577	2	4.0	12.001	15.8088
58	1.31	27.0	24.0	50	0.6	0.577	2	3.0	5.220	28.7044
59	1.12	23.6	22.8	50	1.0	0.839	2	4.0	9.356	25.2127
60	1.31	25.3	22.8	50	0.6	0.839	3	3.0	4.445	58.7498
61	1.12	25.3	22.8	40	1.0	0.577	2	5.0	19.994	12.1399
62	1.31	27.0	22.8	60	0.6	0.577	1	4.0	11.000	32.8857
63	1.31	23.6	22.8	40	0.8	0.364	2	3.0	3.8281	20.9634
64	3.00	25.3	24.0	50	0.6	0.577	1	4.0	22.353	9.6974
65	1.31	27.0	22.8	40	0.6	0.577	3	4.0	12.130	23.7157
66	3.00	25.3	21.6	50	1.0	0.577	1	4.0	25.955	13.9854
67	1.31	25.3	22.8	50	1.0	0.839	1	3.0	9.995	38.4399
68	1.31	25.3	22.8	50	1.0	0.364	3	3.0	9.508	20.4810
69	1.31	23.6	22.8	60	1.0	0.577	1	4.0	11.439	29.9427
70	3.00	27.0	21.6	40	0.8	0.577	2	4.0	13.031	16.3864
71	3.00	27.0	22.8	50	0.8	0.577	1	3.0	23.536	18.7306
72	1.12	25.3	22.8	40	0.6	0.577	2	3.0	14.766	23.6030
73	3.00	25.3	22.8	60	1.0	0.577	2	5.0	12.625	15.4131
74	1.12	25.3	22.8	40	0.8	0.839	3	4.0	16.964	21.6084
75	3.00	23.6	22.8	50	0.8	0.577	1	5.0	36.288	21.9025
76	1.31	25.3	21.6	40	0.8	0.577	1	3.0	17.429	15.9320
77	3.00	25.3	21.6	50	0.6	0.577	3	4.0	9.594	24.3127
78	1.31	27.0	22.8	60	0.8	0.364	2	3.0	1.926	32.7075
79	1.31	25.3	22.8	50	0.6	0.839	1	5.0	26.159	40.8596
80	1.31	25.3	24.0	60	0.8	0.577	1	3.0	13.561	23.5279
81	3.00	25.3	22.8	60	0.8	0.364	1	4.0	12.061	20.2670
82	1.31	25.3	21.6	40	0.8	0.577	3	5.0	13.791	21.7346
83	1.31	25.3	24.0	60	0.6	0.364	2	4.0	10.214	15.6993
84	1.31	25.3	22.8	50	0.8	0.577	2	4.0	43.547	12.0032
85	3.00	23.6	22.8	50	1.0	0.364	2	4.0	14.184	12.7931
86	1.31	23.6	21.6	50	1.0	0.577	2	5.0	13.129	13.6382
87	1.31	25.3	22.8	50	0.6	0.364	1	3.0	14.499	14.0604
88	3.00	23.6	22.8	50	0.6	0.839	2	4.0	14.039	12.3943
89	1.12	25.3	22.8	40	0.8	0.364	1	4.0	14.051	16.0249
90	1.31	25.3	22.8	50	0.8	0.577	2	4.0	15.807	25.7049
91	1.31	25.3	21.6	60	0.8	0.577	3	3.0	4.583	41.7071
92	3.00	25.3	24.0	50	0.8	0.364	2	3.0	11.058	15.5692
93	1.31	25.3	24.0	60	1.0	0.839	2	4.0	7.876	21.4320
94	1.12	25.3	24.0	50	0.6	0.577	3	4.0	5.316	44.7676
95	1.31	27.0	21.6	50	0.8	0.364	3	4.0	10.903	23.7311
96	1.31	23.6	22.8	60	0.6	0.577	3	4.0	7.9018	28.0001
97	1.31	25.3	21.6	60	0.6	0.839	2	4.0	7.151	23.0684
98	1.31	23.6	21.6	50	0.8	0.839	3	4.0	11.730	20.9055

Table 4 (continued)

No.	*A* (GPa)	*B* (MPa)	*C* (MPa)	*D*	*E* (GPa)	*F*	*G*	*H* (10^{-8} m/step)	*M* (GPa)	*U* (μJ/mm^3)
99	3.00	23.6	22.8	50	0.8	0.577	3	3.0	13.022	24.5573
100	1.12	25.3	22.8	60	0.8	0.364	3	4.0	4.406	29.6326
101	3.00	25.3	22.8	40	0.6	0.577	2	5.0	18.855	16.2142
102	3.00	25.3	21.6	50	0.8	0.364	2	5.0	18.673	11.4204
103	1.31	23.6	24.0	50	0.6	0.577	2	5.0	12.488	24.8487
104	1.12	25.3	24.0	50	1.0	0.577	1	4.0	20.287	12.9523
105	1.31	25.3	22.8	50	0.8	0.577	2	4.0	20.548	19.1037
106	1.12	27.0	24.0	40	0.8	0.577	2	4.0	10.443	15.6242
107	1.12	27.0	22.8	50	1.0	0.364	2	4.0	10.622	27.0151
108	3.00	23.6	21.6	60	0.8	0.577	2	4.0	10.174	25.4238
109	1.31	23.6	22.8	40	0.8	0.839	2	5.0	14.549	16.6446
110	1.12	25.3	22.8	60	0.6	0.577	2	5.0	10.379	14.0986
111	1.12	27.0	21.6	60	0.8	0.577	2	4.0	11.723	18.0587
112	1.31	23.6	21.6	50	0.6	0.577	2	3.0	1.8504	27.5298
113	1.12	23.6	21.6	40	0.8	0.577	2	4.0	17.571	17.5165
114	1.12	23.6	22.8	50	0.8	0.577	3	5.0	16.791	14.4502
115	1.12	25.3	21.6	50	0.8	0.839	2	5.0	13.197	24.3039
116	1.12	25.3	21.6	50	1.0	0.577	3	4.0	10.273	39.0787
117	1.31	23.6	22.8	60	0.8	0.364	2	5.0	10.444	17.3895
118	1.31	25.3	22.8	50	1.0	0.839	3	5.0	12.631	30.6712
119	1.12	25.3	21.6	50	0.6	0.577	1	4.0	12.140	17.0884
120	1.31	25.3	24.0	40	0.6	0.839	2	4.0	8.019	22.5002

Table 5 Variance analysis of regression model for evaluating factors affecting the post peak modulus

Item	Sum of squares	df	Mean square	*F* Value	*P*-value	Note
Model	2632.28	8	329.04	10.95	< 0.0001	Significant
A-PBM deformation modulus	280.83	1	280.83	9.35	0.0028	
B-PBM tensile strength	16.59	1	16.59	0.55	0.4590	
C-PBM cohesion	16.83	1	16.83	0.56	0.4557	
D-SJM DFN density	666.68	1	666.68	22.19	< 0.0001	
E-SJM shear stiffness	94.28	1	94.28	3.14	0.0792	
F-SJM friction coefficient	1.68	1	1.68	0.056	0.8134	
G-Height-to-diameter ratio	901.40	1	901.40	30.00	< 0.0001	
H-Loading rate	653.99	1	653.99	21.77	< 0.0001	
Residual	3334.76	111	30.04			
Lack of fit	2399.85	104	23.08	0.17	0.7519	Not significant
Cor total	5967.04	119				

3.1 Effect of a single factor on M of coal samples

The mechanical response of coal samples under uniaxial compression is determined by the mechanical properties, size, and shape of the specimen as well as the loading conditions. As shown in Table 5, DFN density, height-to-width ratio, and loading rate have a significant effect on *M*, while the PBM deformation modulus has a less significant effect. Based on the analysis presented in Sect. 2, these four factors are important characterization parameters of coal matrix, structural surface characteristics, model size, and loading conditions. Therefore, they were selected to investigate their effects on *M*.

For convenience in subsequent discussions, the median value of each influencing factor parameter was defined as the parameter when the coded value is 0. Specifically, the median values of deformation modulus, tensile strength, cohesion of PBM, DFN density, shear modulus, friction

coefficient of SJM, height-to-width ratio, and loading rate parameters are 1.31 GPa, 25.3 MPa, 22.8 MPa, 50, 0.8 GPa, 0.577, 2.0, and 4.0×10^{-8} m/step, respectively.

Figure 4 illustrates the influence of a single factor on M of coal samples. The black solid line represents the predicted M trend with influencing factors, while the red dashed line denotes the least significant difference (LSD) curve, which is affected by the model design and confidence interval. When the variance analysis shows that the regression effect of the model design is significant, the LSD curve does not cross, indicating a significant difference in the prediction results.

The deformation resistance of coal matrix particles is regulated by the PBM deformation modulus, which is positively correlated with the stiffness of the numerical core. As shown in Fig. 4a, when other factors are fixed at their median values, *M* of the numerical core increases approximately linearly with the deformation modulus of the PBM. A high deformation modulus of the PBM model promotes post-peak brittleness, where the tips of the primary defects are the first to break under the external load, followed by interconnecting and coalescing to form a main fracture surface. With an increase in DFN density, the internal damage morphology of the specimen becomes more complex, leading to a step-like

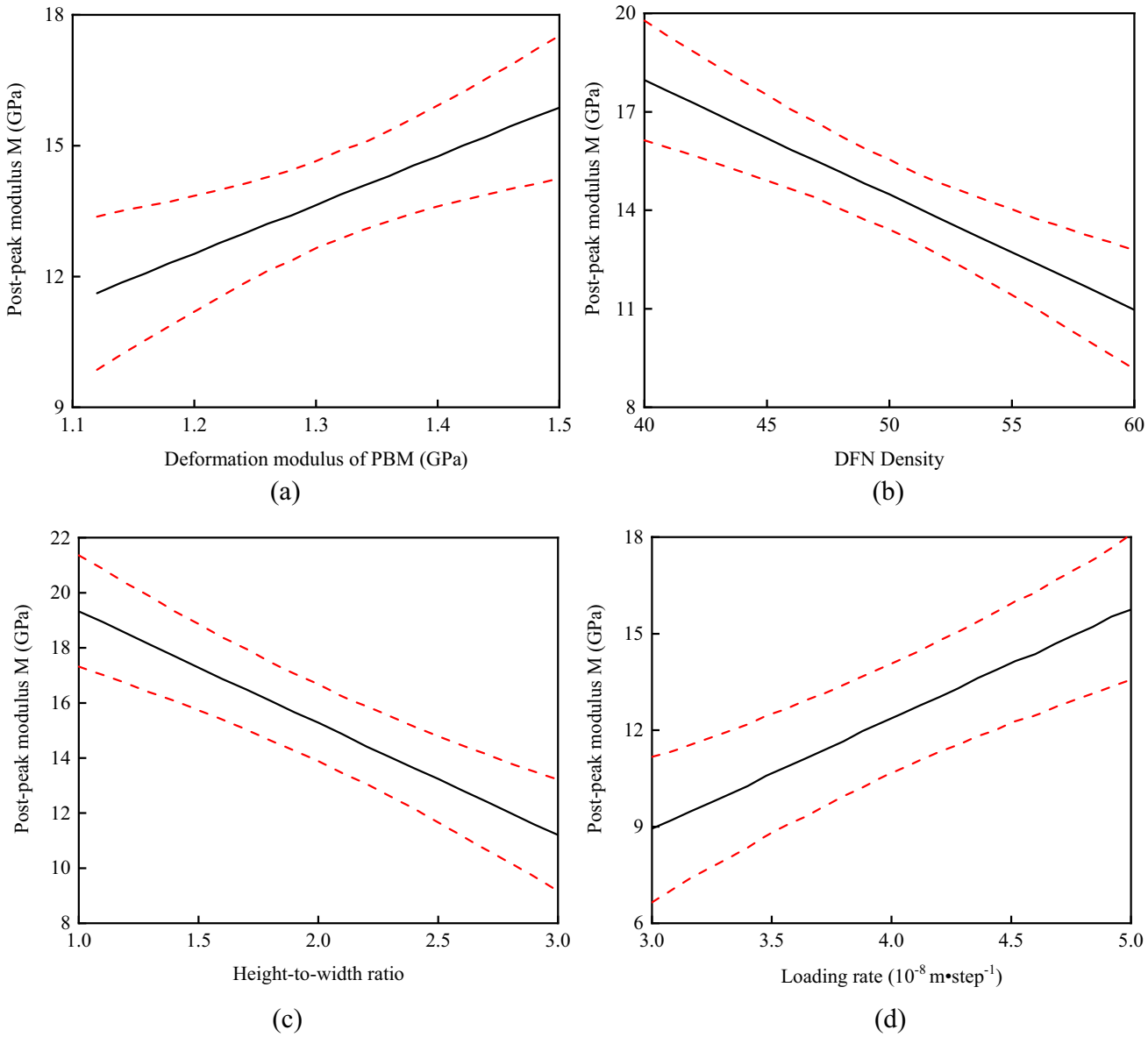

Fig. 4 Influence of single factor on the post-peak modulus of coal under unconfined compression. **a** Deformation modulus of PBM, **b** DFN density, **c** Height-to-diameter ratio, and **d** Loading rate

decline in the post-peak section of the stress–strain curve, an increase in the proportion of the post-peak section of the stress–strain curve, and a decrease in *M*.

Table 5 indicates that the height-to-width ratio and loading rate have a highly significant effect on *M*. Under uniaxial compression, *M* decreases approximately linearly with an increase in the height-to-width ratio. This can be explained from two aspects: (1) The current simulation adopts the method of adjusting the height of the model by fixing the diameter to modify the height-to-width ratio, resulting in a linear and positive correlation between specimen size and the height-to-width ratio. When the DFN density is fixed, an increase in the height-to-width ratio results in more fractures contained in the specimen, making the post-peak feature of the stress–strain curve more complex, increasing the proportion of the post-peak section of the stress–strain curve, and decreasing *M*; (2) As the specimen height increases, for the same loading rate, the strain rate decreases, and the post-peak brittle feature weakens, resulting in a decrease in *M*. By increasing the loading rate, the brittleness of the specimen is enhanced, resulting in an increase in *M*, as shown in Fig. 4d.

3.2 Effect of multi-factor interactions on *M* of coal samples

The mechanical behavior of coal specimens under compression is the result of the interaction of multiple factors. As shown in Sect. 3.1, the PBM deformation modulus, SJM DFN density, height-to-width ratio, and loading rate significantly affect *M* of coal samples, representing coal matrix properties, structural plane characteristics, model size characteristics, and loading conditions, respectively. In this section, we analyze the interactions of these four factors and their impact on *M* of coal samples.

Figure 5 depicts the influence of interactions among PBM deformation modulus, SJM DFN density, height-to-width ratio, and loading rate on *M*, with other factors fixed at their median values. A comparison of Figs. 4 and 5 shows that the influence trend of multi-factor interactions on *M* is consistent with that of a single factor. Specifically, *M* is positively correlated with the PBM deformation modulus and loading rate, and negatively correlated with SJM DFN density and the height-to-width ratio.

The contour lines in the response surface represent the curvature of the response surface, with more compact contour lines indicating a more significant impact on M. The contour lines in Fig. 5 are mostly located in the middle, indicating that the response surface's curvature increases and then decreases, resulting in an "S" shape. Figure 5a–f illustrate the impact of the interactions of PBM deformation modulus, SJM DFN density, height-to-width ratio, and loading rate on *M* of coal samples. The projection contour lines of the response surface are evenly distributed when the PBM deformation modulus increases, indicating that the change of PBM deformation modulus has a less interfering effect on other influencing factors. Figure 5a shows that the decrease rate of *M* slows down as SJM DFN density increases when the PBM deformation modulus is low (i.e., 1.12 GPa), while the reduction rate of *M* increases with SJM DFN density when the PBM deformation modulus is higher (i.e., 1.50 GPa). Figure 5b shows that the decreasing rate of *M* slows down as the height-to-width ratio increases when the PBM deformation modulus is low, while the reduction rate of *M* increases with the height-to-width ratio when the PBM deformation modulus is higher. Figure 5c shows that the increase rate of *M* increases with loading rate when the PBM deformation modulus is low, while the increase rate of *M* slows down as the loading rate increases when the PBM deformation modulus is higher.

Figure 5d, e illustrate the influence of SJM DFN density on M of coal samples when interacting with the height-to-width ratio and loading rate, respectively. When the DFN density is 60, the contour lines of the response surface projection are more compact, indicating that changes in the height-to-width ratio and loading rate have a more significant effect on M when the DFN density is higher. Figure 5e, f show that the contour lines of the response surface projection are more compact when the loading rate is low (i.e., 3.0×10^{-8} m/step), indicating that changes in SJM DFN density and the height-to-width ratio have a more significant effect on *M* when the loading rate is low.

4 Analysis of factors influencing the post-peak energy density *U*

Table 6 presents the results of the variance analysis of the regression model for factors influencing *U*. A *P* value less than 0.0001 indicates that the regression effect is highly significant. The *F* value is inversely related to the *P* value in the regression model, and the height-to-width ratio has the largest *F* value, indicating that it has the most significant effect on *U* among the eight factors considered. The sensitivity of the response of *U* to the four highly significant factors decreases in the following order: height-to-width ratio > loading rate > PBM deformation modulus > SJM DFN density.

4.1 Effect of a single factor on *U* of coal samples

Figure 6 illustrates the influence of each factor on *U* of coal samples. The PBM deformation modulus regulates the ability of coal matrix particles to resist deformation, meaning that the numerical core stiffness is positively related to the PBM deformation modulus. As depicted in Fig. 6a, when the other factors are constant and at intermediate levels, *U*

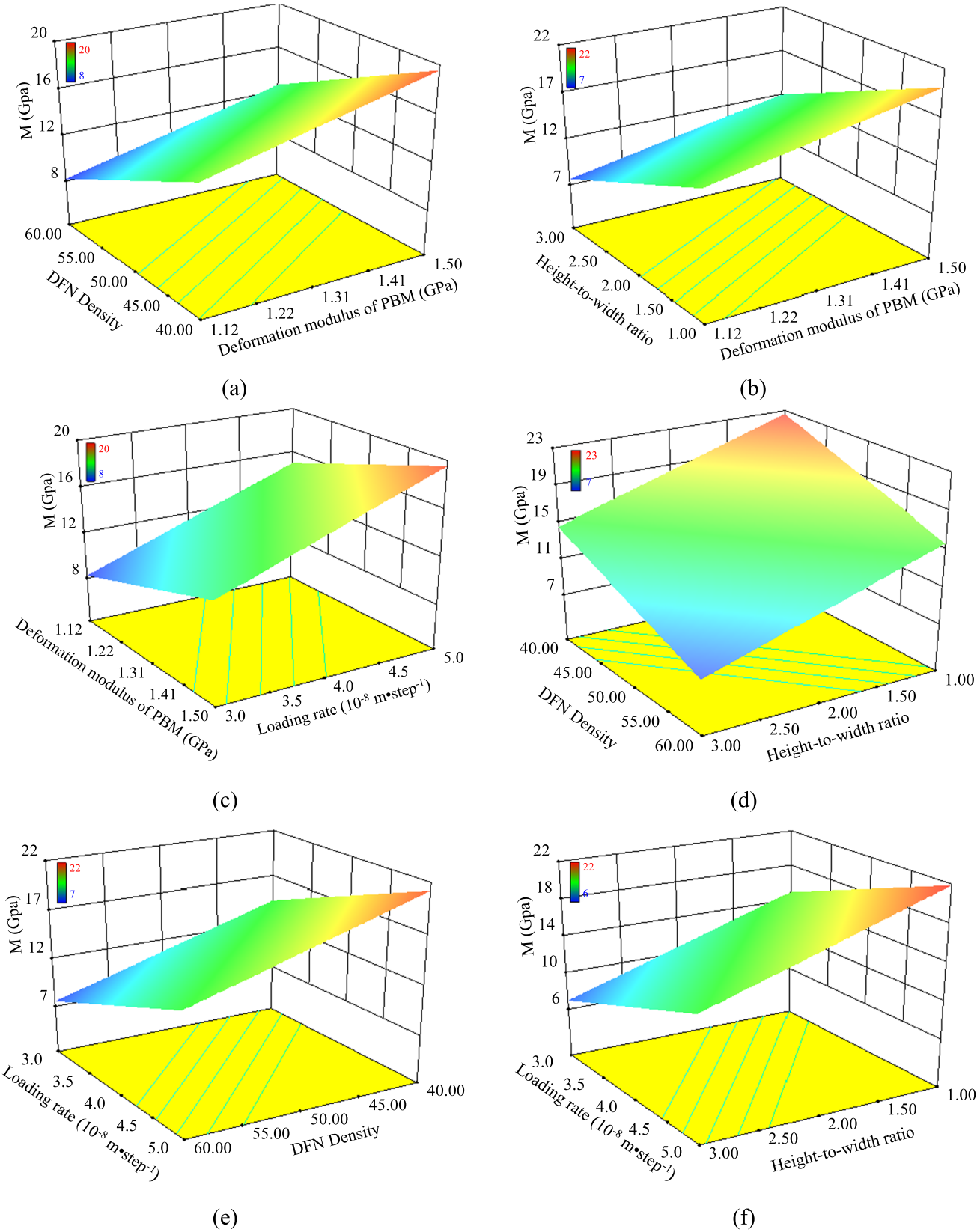

Fig. 5 The interaction influence of multi factor on the post-peak modulus *M* of coal under unconfined compression. **a** Deformation modulus of PBM and DFN density, **b** Deformation modulus of PBM and—height-to-width ratio, **c** Deformation modulus of PBM and loading rate, **d** DFN density and height-to-width ratio, **e** DFN density and loading rate, and **f** height-to-width ratio and loading rate

Table 6 Variance analysis of regression model for evaluating factors affecting the post peak energy density

Item	Sum of squares	df	Mean square	*F* value	*P*-value	Note
Model	46.2	8	5.78	10.39	< 0.0001	Significant
A-PBM deformation modulus	9.00	1	9.00	16.18	0.0001	
B-PBM tensile strength	0.63	1	0.63	1.12	0.2912	
C-PBM cohesion	0.02	1	0.02	0.035	0.8511	
D-SJM DFN density	8.83	1	8.83	15.88	0.0001	
E-SJM shear stiffness	1.10	1	1.10	1.98	0.1617	
F-SJM friction coefficient	4.85	1	4.85	8.73	0.0038	
G-Height-to-diameter ratio	12.48	1	12.48	22.44	< 0.0001	
H-Loading rate	9.29	1	9.29	16.71	< 0.0001	
Residual	61.72	111	0.56			
Lack of fit	56.68	104	0.55	0.76	0.7519	Not significant
Cor total	107.92	119				

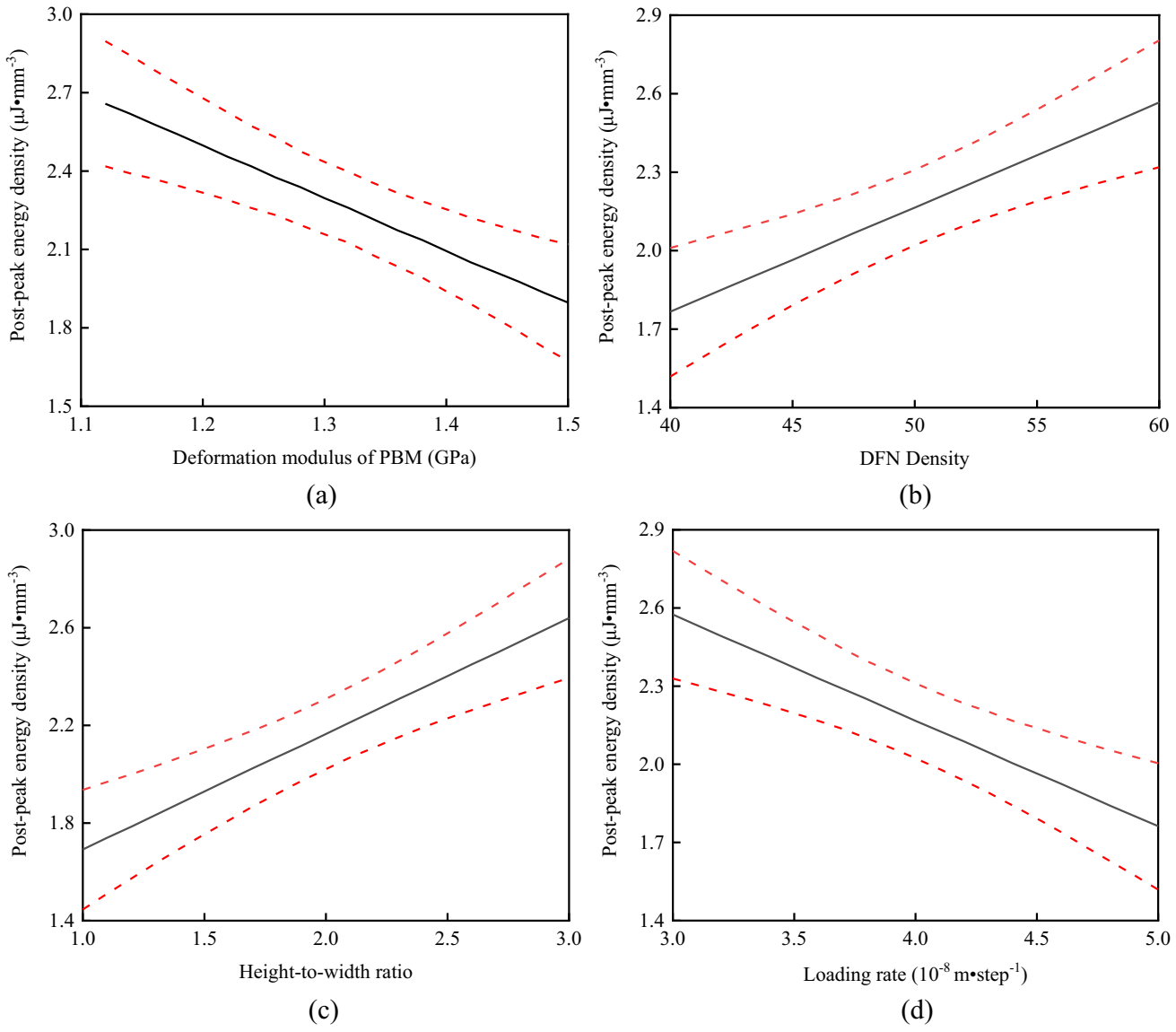

Fig. 6 Influence of single factor on the post-peak energy density of coal under unconfined compression. **a** Deformation modulus of PBM, **b** DFN density, **c** Height-to-width ratio, **d** Loading rate

decreases approximately linearly with the PBM deformation modulus. As analyzed in Sect. 2.1, the mechanical parameters of the primary defects are much lower than those of the coal matrix, and failures occur initially at the tips of the primary defects, followed by interconnection and coalescence to form the main fracture surface. With the increase of SJM DFN density, the damage morphology inside the specimen becomes more intricate when the load reaches the ultimate bearing capacity of the sample. As a result, there is a step-like decline in the post-peak section of the stress–strain curve, an increase in the proportion of the post-peak section of the stress–strain curve, and an increase in U. Another factor that has a significant effect on U is the height-to-width ratio, as shown in Table 6. When other factors are at intermediate levels and constant, U increases approximately linearly with the height-to-width ratio. This result can be explained by two aspects: (1) When the DFN density is constant, cracks in the specimen increase with the height-to-width ratio, resulting in a more complicated post-peak stress–strain curve. (2) The strain rate decreases with increasing specimen height, leading to a decrease in post-peak brittleness at the same loading rate and an increase in U. Conversely, the brittleness of the sample increases as the loading rate increases, leading to a decrease in U, as depicted in Fig. 6d.

4.2 Effect of multi-factor interactions on *U* of coal samples

The interactions of the PBM deformation modulus, the SJM DFN density, the height-to-width ratio, and the loading rate on U are presented in Fig. 7, with tensile strength and cohesion of PBM, shear modulus, and friction coefficient of SJM set at intermediate levels. The influence of multi-factor interactions on U is consistent with that of a single factor. Specifically, U of the coal samples is negatively correlated with the PBM deformation modulus and the loading rate, and positively correlated with the SJM DFN density and the height-to-width ratio.

Figures 7a–c illustrate the impact of the interactions among the PBM deformation modulus, SJM DFN density, height-to-width ratio, and loading rate on U of coal samples. Unlike Figs. 7d–f, the contour lines projected on the response surface in Figs. 7a–c are not uniformly distributed, but rather concentrated on one side, indicating that the influence of DFN density, height-to-width ratio, and loading rate on U changes with the PBM deformation modulus. This suggests that the PBM deformation modulus and other influencing factors have significant interaction effects on U of the coal samples. When the PBM deformation modulus is 1.50 GPa, the contour lines projected on the response surface are more compact, indicating that the SJM DFN density, height-to-width ratio, and loading rate have more significant effects on U of the numerical cores.

The contour lines projected on the response surface in Figs. 7d–f are almost uniformly distributed, indicating that there is little interaction among the DFN density, height-to-width ratio, and loading rate of SJM. The overall density of the contour lines projected on the response surface in Figs. 7d–f is higher than that in Figs. 7a–c, indicating that the influence of the DFN density, height-to-width ratio, and loading rate on U is more significant.

The degree of distortion of the response surface can reflect the intensity of the interaction between different factors (Tao et al. 2016). The response surface under the interaction of multiple factors in Figs. 5 and 7 are not plans, indicating that the interaction of different factors affects the response values (M and U). However, the degree of distortion of the response surface is relatively low, indicating that the interaction between different factors is not significant. The reason for the small interaction is that a certain factor is the representation of a single attribute of numerical core, and the change of a certain factor is difficult to affect the role of other factors, that is, the independence of each factor is strong.

5 Insight into coal burst prevention

5.1 Suggested measures for coal burst prevention

Based on the analyses presented in Sects. 3 and 4, coal burst prevention can be approached from four different aspects: (1) mechanical properties of the coal matrix, (2) characteristics of the structural weak planes, (3) width of the coal pillar and mining layout, and (4) advance speed of the working face.

(1) Weakening the mechanical parameters of coal.

The pre-peak energy accumulation of coal samples decreases as the strength decreases. The slope of the line between peak strength and residual strength also decreases, resulting in a reduction in M. As the mechanical properties of the coal sample matrix decrease, the post-peak energy dissipation increases, prolonging the post-peak section of the stress–strain curve, which in turn prolongs failure time. This results in a reduction in effective residual energy that can be converted into coal ejection and a decrease in the conversion rate. The softening and dissolution of water can decrease the mechanical properties of coal and alter its failure mode. As water content increases, the strength and elastic modulus of coal decrease, and the loaded accumulated elastic strain energy also decreases. Meanwhile,

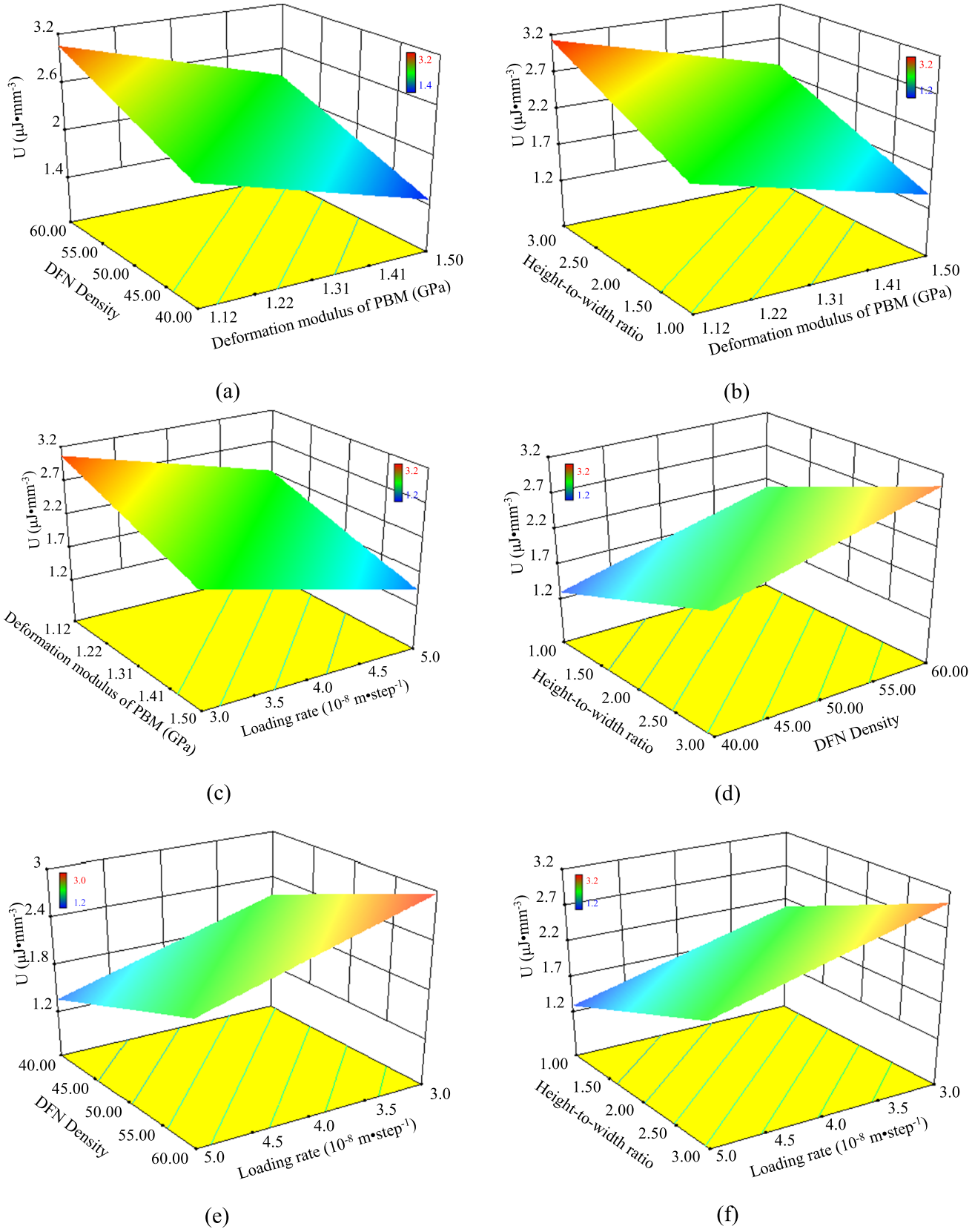

Fig. 7 The interaction influence of multi factor on the post-peak energy density *U* of coal under unconfined compression. **a** Deformation modulus of PBM and DFN density, **b** Deformation modulus of PBM and height-to-width ratio, **c** Deformation modulus of PBM and loading rate, **d** The DFN density and height-to-width ratio, **e** DFN density and loading rate, and **f** Height-to-width ratio and loading rate

permanently dissipated energy increases due to plastic deformation, resulting in decreased bursting liability. Therefore, injecting water to soften the coal body is the most commonly used and effective measure for the prevention and control of coal burst in coal mines.

(2) Increasing the number of structural weak surfaces.

The density of DFN in SJM reflects the distribution pattern of the structural weak surface in coal. Due to the lower mechanical parameters of the structural weak surface compared to the matrix, the characteristics of the structural weak surface significantly affect the mechanical behavior of coal samples under uniaxial compression. The increase in DFN density of the SJM model corresponds to the increase in the number of structural weak planes in actual coal samples. On one hand, the strength of the coal body significantly decreases, and the pre-peak energy accumulation decreases. On the other hand, the post-peak energy dissipation increases, resulting in a significant decrease in the effective residual energy converted into coal sample failure and debris ejection. Additionally, with the increase in the structural weak surface, the post-peak section of the stress–strain curve shows a step-like decline, and the failure time prolongs. Thus, the rate of effective residual energy conversion into the kinetic energy of coal ejection reduces, and the risk of coal burst weakens. In practical production, techniques such as deep hole blasting to loosen coal and rock, drilling to increase coal porosity, and hydraulic fracturing can be used to generate more structural weak surfaces in coal and reduce the possibility and impact of coal burst.

(3) Reducing the width of the coal pillars.

The study has demonstrated that an increase in the height-to-width ratio leads to a decrease in the strength of specimens and energy accumulation before failure. As discussed in Sects. 2 and 3, M of the sample is negatively correlated with the height-to-width ratio, while the post-peak energy density U is positively correlated with it. As the height-to-width ratio of the sample increases, the post-peak energy dissipation also increases, resulting in a significant decrease in the effective residual energy that can be transformed into coal sample failure and debris ejection, and ultimately reducing the risk of coal burst. The height of the coal pillar is often constrained by the thickness of the coal seam and mining height, which makes it challenging to adjust. However, the width of the coal pillar can be reduced to adjust the height-to-width ratio. Therefore, reducing the width of the coal pillar is an effective measure to prevent coal burst, and the use of small coal pillars has become widely adopted in coal mines for this purpose.

(4) Optimizing the mining replacement and speed.

The process of roadway driving and working face mining transfers the load of the overlying strata to the unmined area. The speed of mining directly affects the rate at which the surrounding rock experiences stress. Optimizing the mining and excavation process, such as avoiding the formation of an island working face, is crucial to improving the surrounding rock stress environment. Maintaining an appropriate mining speed is a basic requirement for optimizing the mining process and directly affects the loading and unloading rate of the coal pillar, making it a significant factor in preventing coal pillar burst.

5.2 A case study

The efficacy of the suggested measures for preventing coal burst was confirmed through a case study conducted at the Hongqinghe Coal Mine. In the first mining area of the south limb of the 3-1 coal seam, the auxiliary transport roadway of working face 3-1103 experienced frequent coal bursts following excavation. To address this issue, large-diameter drilling technology was utilized in the entries of the working face to damage the coal on both sides, with the aim of weakening the mechanical properties of the coal. The construction location is depicted in Fig. 8. The drilling holes, which had a diameter of 153 mm, were arranged in a single-row with a spacing of 1.0 m. The coal pillar wall hole spanned 18 m, while the non-coal pillar wall was 20 m. The vertical roadway wall inclined upwards at an angle of 3°–5°.

5.3 Verification of prevention and control effect

The effectiveness of the implemented measures for coal burst prevention was evaluated by comparing the microseismic data and coal volume obtained from probe drilling.

(1) Microseismic Events.

To analyze the distribution of microseismic events, data was selected from before the construction of large-diameter boreholes and from the first, third, and fifth weeks after construction, as shown in Fig. 9. Comparison of Fig. 9a with b–d indicates that prior to the construction of boreholes, the frequency and energy of microseismic events were relatively high. Within 1 week before construction, more than 100 microseismic events were detected, including two large events with energy greater than 10^5 J. The maximum energy recorded was 4.2×10^6 J. Following the construction of large-diameter boreholes, the frequency and energy of microseismic events in the area significantly decreased. Within 6 weeks after the construction, only 42 microseismic events were recorded, with most of the events having small

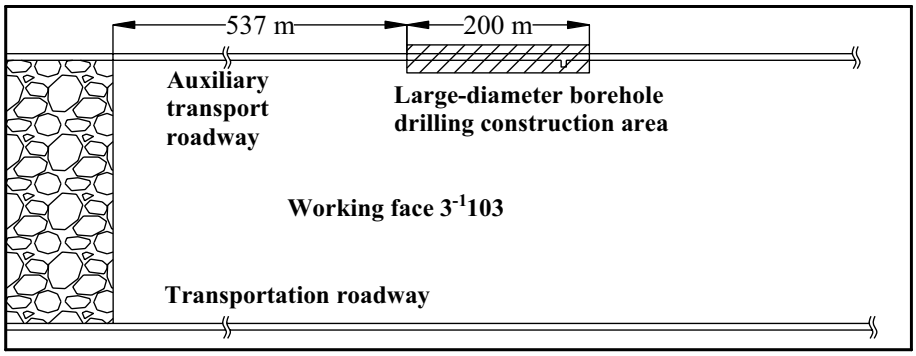

Fig. 8 Large-diameter borehole drilling construction area

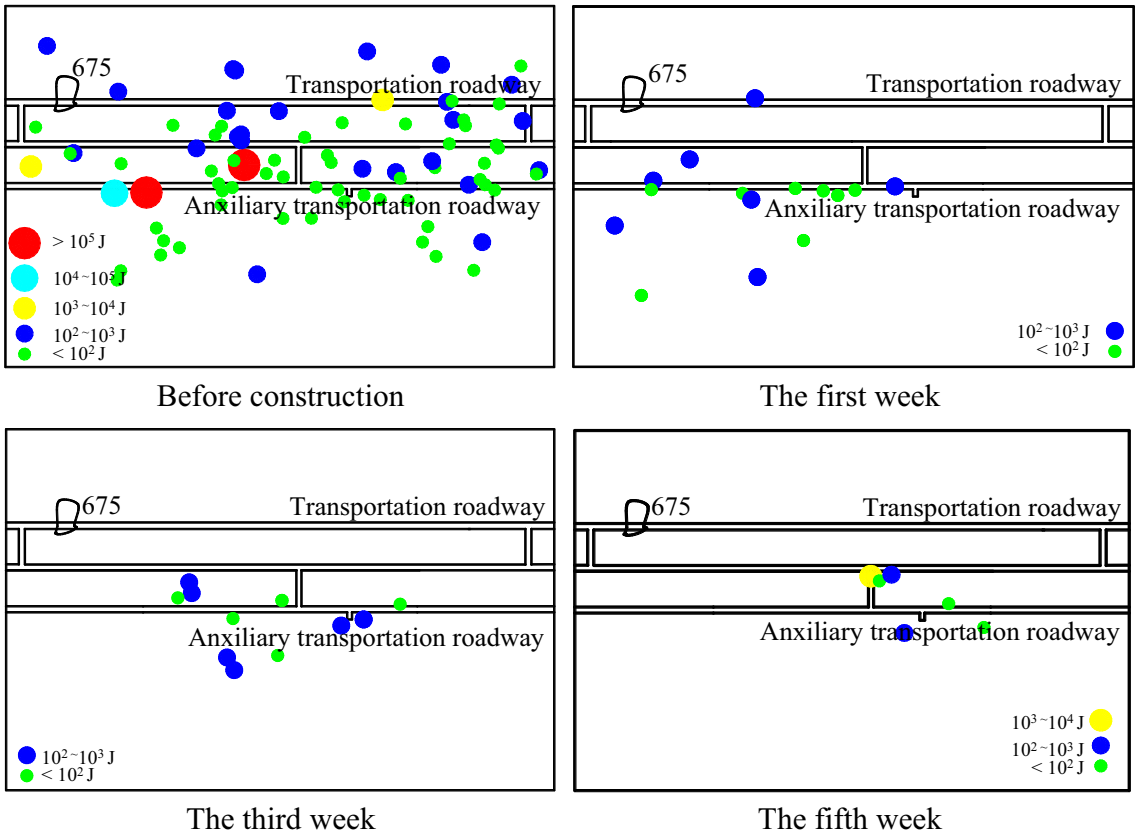

Fig. 9 Distribution of the microseismic events before and after large-diameter borehole drilling

energy of less than 1000 J. The maximum energy recorded was 8.89×10^3 J, which was significantly lower than that of microseismic events before borehole drilling.

The effectiveness of the measures adopted for coal burst prevention was confirmed through a comparison of microseismic data and coal volume obtained from probe drilling. The microseismic events before and after the construction of large-diameter boreholes were analyzed to evaluate their effectiveness in mitigating coal burst. Figure 9 shows the distribution of microseismic events before borehole drilling construction and during the first, third, and fifth weeks after construction.

Comparing Fig. 9a with b–d, it is evident that the frequency and energy of microseismic events were relatively high before the construction of large-diameter boreholes. Over 100 microseismic events were detected within 1 week before construction, including two large events with energy greater than 10^5 J. The maximum energy recorded was 4.2×10^6 J. After the construction of large-diameter boreholes, the frequency and energy of microseismic events in the area decreased

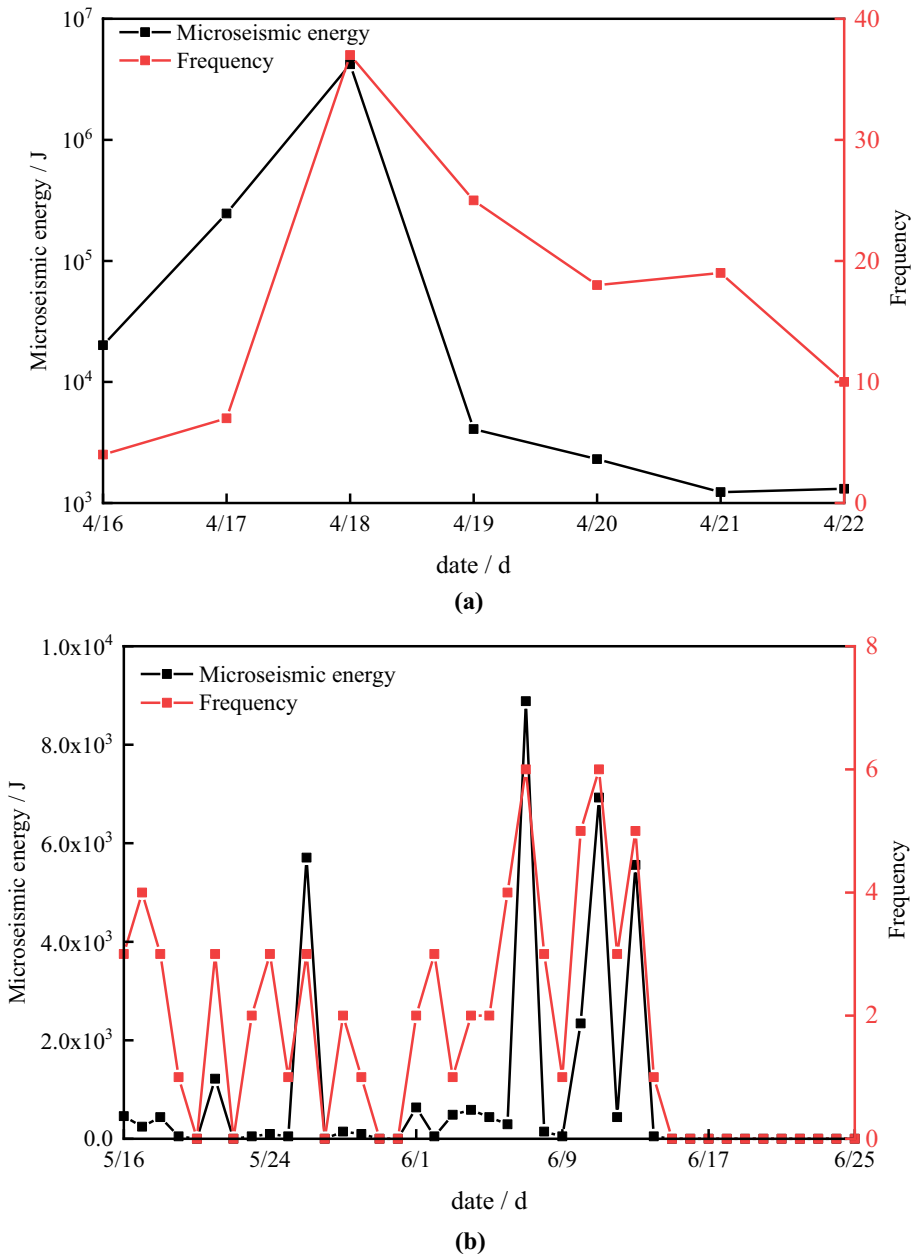

Fig. 10 Evolution of microseismic energy and frequency. **a** Microseismic energy and frequency before large-diameter borehole drilling, and **b** Microseismic energy and frequency after large-diameter borehole drilling

significantly. Only 42 microseismic events were monitored within 6 weeks after construction, with most events having small energy of less than 1000 J. The maximum energy recorded was 8.89×10^3 J, which was significantly lower than that of microseismic events before large-diameter borehole drilling.

After the construction was completed, high-energy microseismic events were mainly distributed in the coal pillar in the pressure relief area. In terms of time, microseismic events occurred sporadically in the first 4 weeks after drilling construction, with low energy levels indicating that the coal pillar in the pressure relief area was damaged during this period, the stress redistributed, and the elastic energy released. However, after the fifth week, there were almost no microseismic events in the pressure relief area, indicating that the mechanical properties of the coal pillar damaged by large-diameter drilling were significantly reduced. After 4 weeks, the stress and energy distribution of the coal pillar reached a stable state again, and the possibility of coal bursts was significantly reduced. The microseismic energy and frequency in this area are shown in Fig. 10. The microseismic energy and daily frequency in the first 4 weeks after the large-diameter drilling were fluctuating. At the fifth week, the microseismic energy and daily frequency in the roadway area were at a very low level, indicating that the coal pillar had reached a stable state.

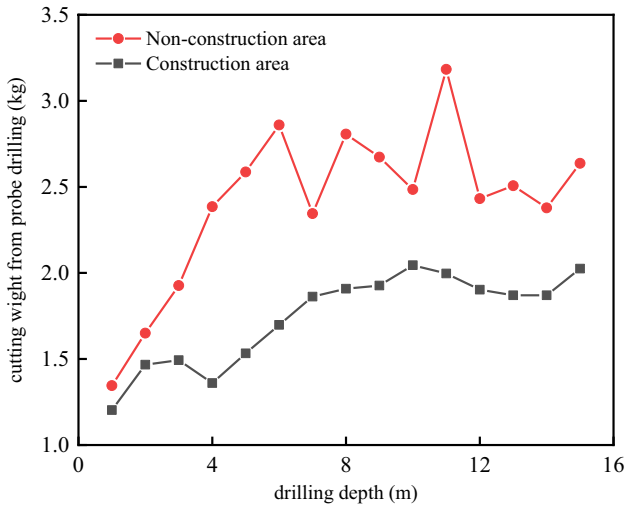

Fig. 11 Effect of large-diameter borehole drilling on the cutting weight from probe drilling

(2) Probe drilling.

Probe drilling is an effective method to identify the highly stressed coal that is prone to bursting (Mark 2021). To investigate the effectiveness of the large-diameter borehole drilling in reducing stress within the coal pillar, two groups of probe drilling were conducted in the auxiliary transport roadway, one in the construction section and the other in the non-construction section. Each group consisted of three boreholes with a diameter of 42 mm, a spacing of 10 m, and a depth of 15 m.

The average weight of the coal cutting from the three boreholes at each location is presented in Fig. 11. During the drilling process, no abnormal situations such as water discharge or drill sticking occurred. The results show that the cutting weight in the construction section was significantly lower than that in the non-construction section, indicating a substantial reduction in stress within the coal pillar due to the large-diameter borehole drilling.

6 Conclusions

In this study, a comprehensive numerical investigation was conducted to identify the key factors influencing the post-peak behavior of coal samples subjected to uniaxial compression. The study considered factors such as the mechanical properties of the coal matrix, characteristics of the structural weak surface, size of coal samples, and loading conditions. Two parameters, namely the post-peak modulus M and post-peak energy density U, were used to evaluate the post-peak characteristics of coal. The analysis revealed that the deformation modulus, DFN density, height-to-width ratio, and loading rate significantly influence the post-peak behavior of coal. A sensitivity analysis was performed, and the following conclusions were drawn:

(1) M is positively correlated with the deformation modulus and loading rate, while it is negatively correlated with the DFN density and height-to-width ratio. The sensitivity of M to each significant factor was found to be in the order of height-to-width ratio > DFN density > loading rate > deformation modulus. The effect of a single factor on M demonstrated a good linear relationship, while M exhibited a trend of increasing first and then decreasing with the response surface curvature of multi-factor interactions. This indicates that the sensitivity of M to influencing factors initially increases and then decreases.

(2) U is negatively correlated with the deformation modulus and loading rate, and negatively correlated with the DFN density and height-to-width ratio. The effect of a single factor on U showed a good linear relationship. The sensitivity of U to each significant influence factor was found to be in the order of height-to-width ratio > loading rate > deformation modulus > DFN density. When the deformation modulus interacted with other factors, the response surface projection contour was concentrated on one side. This indicates that the deformation modulus has a remarkable interaction with other factors on U of coal samples.

(3) Based on the numerical results, several measures for coal burst prevention were proposed, including weakening the mechanical properties of coal, increasing the number of structural weak planes in coal, reducing the width of coal pillar, and optimizing the layout and speed of mining. The effectiveness of the measure to weaken the mechanical properties of coal was successfully verified through a case study.

Acknowledgements The authors have no real or perceive conflicts of interest. This work has been supported by the National NaturalScience Foundation of China (52074151, 52274085, 52274123) and Tiandi Science and Technology Co., Ltd. Science and Technology Innovation Venture Capital Special Project (TDKC-2022-MS-01, TDKC-2022-QN-01, TDKC-2022-QN-02).

References

Ai C, Zhang J, Li Y, Zeng J, Yang X, Wang J (2016) Estimation criteria for rock brittleness based on energy analysis during the rupturing process. Rock Mech Rock Eng 49(12):4681–4698

Akdag S, Karakus M, Nguyen GD, Taheri A, Bruning T (2019) Evaluation of the propensity of strain burst in brittle granite based on post-peak energy analysis. Undergr Space 6(1):1–11

Alonso E, Alejano L, Varas F, Fdez-Manin G, Carranza-Torres C (2003) Ground response curves for rock masses exhibiting strain-softening behaviour. Int J Numer Anal Meth Geomech 27:1153–1185

Cai M, Kaiser P, Tasaka Y, Minami M (2007) Determination of residual strength parameters of jointed rock masses using the GSI system. Int J Rock Mech Min Sci 44:247–265

Cheng C (2011) Influence of discontinuities on post-peak behavior of rock in uniaxial compressive test by numerical study. In: International conference on multimedia technology; Hangzhou, IEEE, pp 6406–6409

Feng GR, Jia XQ, Guo YX, Qi TY, Li Z, Li JZ, Kang LX, Liu GY, Song KG (2016) Study on mixture ratio of gangue-waste concrete cemented paste backfill. J Min Saf Eng 33(6):1072–1079

Gao F, Kang H, Lou J, Li J, Wang X (2019) evolution of local mine stiffness with mining process: insight from physical and numerical modeling. Rock Mech Rock Eng 52(10):3947–3958

Hajiabdolmajid V, Kaiser PK, Martin CD (2002) Modelling brittle failure of rock. Int J Rock Mech Min 39(6):731–741

Han J, Li S, Li S, Wang L (2012) Post-peak stress-strain relationship of rock mass based on Hoek–Brown strength criterion. Proc Earth Planet Sci 5:289–293

Itasca Consulting Group Inc (2016) PFC2D (Particle Flow Code in 2Dimensions) manual, version 5.0. Minneapolis, Minnesota

Jarvie D, Hill R, Ruble T, Pollastro R (2007) Unconventional shale-gas systems: the Mississippian Barnett Shale of northcentral Texas as one model for thermogenic shale-gas assessment. AAPG Bull 9(4):475–499

Kivi IR, Ameri M, Molladavoodi H (2018) Shale brittleness evaluation based on energy balance analysis of stress–strain curves. J Petrol Sci Eng 167:1–19

Kuang Z, Qiu S, Li S, Du S, Huang Y, Chen X (2021) A new rock brittleness index based on the characteristics of complete stress-strain behaviors. Rock Mech Rock Eng 54(3):1109–1128

Li D, Feng GR, Guo YX, Qi TY, Jia XQ, Feng JR, Li Z (2016) Analysis on the strength increase law of filling material based on response surface method. J China Coal Soc 41(2):392–398

Li YW, Long M, Zuo L, Li W, Zhao W (2018) Brittleness evaluation of coal based on statistical damage and energy evolution theory. J Petrol Sci Eng 172:753–763

Liu X, Zhang Z, Ge Z, Zhong C, Liu L (2021) Brittleness evaluation of saturated coal based on energy method from stress–strain curves of uniaxial compression. Rock Mech Rock Eng 54(6):3193–3207

Lu Z, Ju W, Wang H, Zheng J, Yi K, Feng Y, Sun L (2019) Experimental study on anisotropic characteristics of impact tendency and failure model of hard coal. Chin J Rock Mech Eng 38(4):757–768

Mark C (2021) Protecting miners from coal bursts during development above historic mine workings in Harlan County, KY. Int J Min Sci Technol 31:111–116. https://doi.org/10.1016/j.ijmst.2020.12.015

Meng Z, Pan J, Liu L, Meng G, Zhao Z (2009) Influence of moisture contents on mechanical properties of sedimentary rock and its bursting potential. Chin J Rock Mech Eng 28(Supp 1):2637–2672

Meng F, Zhou H, Zhang C, Xu R, Lu J (2014) Evaluation methodology of brittleness of rock based on post-peak stress-–strain curves. Rock Mech Rock Eng 48(5):1787–1805

Peng J, Rong G, Cai M, Yao M, Zhou C (2016) Physical and mechanical behaviors of a thermal-damaged coarse marble under uniaxial compression. Eng Geol 200:88–93

Peng J, Cai M, Rong G, Yao M, Jiang Q, Zhou C (2017) Determination of confinement and plastic strain dependent post-peak strength of intact rocks. Eng Geol 218:187–196

Salamon MDG (1970) Stability, instability and design of pillar workings. Int J Rock Mech Min Sci Geomech Abstr 7:613–631

Tao YJ, Zhu XN, Tao DP, Deng MR, Zhang XB (2016) Optimization of triboelectrostatic decarbonization experiment of fly ash by design-expert. J China Coal Soc 41(2):475–482

Tarasov BG, Potvin Y (2013a) Absolute, relative and intrinsic rock brittleness at compression. Min Technol 121(4):218–225

Tarasov BG, Potvin Y (2013b) Universal criteria for rock brittleness estimation under triaxial compression. Int J Rock Mech Min 59:57–69

Tarasov BG, Randolph MF (2011) Superbrittleness of rocks and earthquake activity. Int J Rock Mech Min 48(6):888–898

Wang F, Gale J (2009) Screening criteria for shale-gas systems. Gulf Coast Assoc Geol Trans 59:779–793

Wang L, Wang HY, Jiang LY (2014) Study of post-peak stress-strain relationship of rock mass with joint. Appl Mech Mater 638–640:561–564

Xia YJ, Li LC, Tang CA, Li XY, Ma S, Li M (2017) A new method to evaluate rock mass brittleness based on stress–strain curves of class I. Rock Mech Rock Eng 50(5):1123–1139

Xu YH, Cai M (2017) Influence of loading system stiffness on post-peak stress–strain curve of stable rock failures. Rock Mech Rock Eng 50(9):2255–2275

Yang S, Jing H, Wang S (2012) Experimental investigation on the strength, deformability, failure behavior and acoustic emission locations of red sandstone under triaxial compression. Rock Mech Rock Eng 45(4):583–606

Yang D, Zhang D, Niu S, Dang Y, Feng W, Ge S (2017) Experiment and study on mechanical property of sandstone post-peak under the cyclic loading and unloading. Geotech Geol Eng 36:1609–1620

Yao M, Rong G, Zhou C, Peng J (2016) Effects of thermal damage and confining pressure on the mechanical properties of coarse marble. Rock Mech Rock Eng 49(6):2043–2054

Zhang H, Li CC (2019) Effects of confining stress on the post-peak behaviour and fracture angle of fauske marble and iddefjord granite. Rock Mech Rock Eng 52(5):1377–1385

Zhang X, Xu J, Sun L, Zang H, Wang Q (2022) Mechanical properties evolution of thermally damaged limestone under triaxial cyclic loading and unloading. J Min Strata Control Eng 4(4):043011

Zhou H, Chen J, Lu J, Jiang Y, Meng F (2018) A new rock brittleness evaluation index based on the internal friction angle and class I stress–strain curve. Rock Mech Rock Eng 51(7):2309–2316